# Shockwave/Boundary-Layer Interaction Studies Performed in the NASA Langley 20-Inch Mach 6 Air Tunnel

Brett F. Bathel,[1] Stephen B. Jones,[2] A. Neal Watkins,[3] Scott A. Berry,[4] Kyle Z. Goodman,[5] William E. Lipford[6]
*NASA Langley Research Center, Hampton, VA, 23681*

Christopher S. Combs[7]
*The University of Texas at San Antonio, San Antonio, TX, 78249*

John D. Schmisseur,[8] Phillip A. Kreth,[9] and E. Lara Lash[10]
*The University of Tennessee Space Institute, Tullahoma, TN, 37388*

**This paper highlights results from a collaborative study performed by The University of Tennessee Space Institute (UTSI) and NASA Langley Research Center on the Shockwave/Boundary-Layer Interaction (SWBLI) generated by a cylindrical protuberance on a flat plate in a Mach 6 flow. The study was performed in the 20-Inch Mach 6 Air Tunnel at NASA Langley Research Center and consisted of two separate entries. In the first entry, simultaneous high-speed schlieren and high-speed pressure-sensitive paint (PSP) imaging – which was performed for the first time in the 20-Inch Mach 6 facility at NASA Langley – were performed as well as simultaneous high-speed schlieren and oil-flow imaging. In the second entry, the model configuration was modified to increase the size of the interaction region. High-speed schlieren and infrared thermography (IR) surface imaging were performed in this second entry. The goal of these tests was to characterize the SBLI in the presence of a laminar, transitional, and turbulent boundary layer using high-speed optical imaging techniques.**

## Nomenclature

| | | |
|---|---|---|
| $AoA$ | = | sting angle-of-attack (°) |
| $d_{cylinder}$ | = | cylinder diameter (mm) |
| $d_{trip}$ | = | cylindrical tripping element diameter (mm) |
| $\Delta_{shock}$ | = | shock stand-off distance (mm) |
| $h_{cylinder}$ | = | cylinder height (mm) |
| $h_{trip}$ | = | cylindrical tripping element height (mm) |
| $HSS$ | = | high-speed schlieren |
| $M_\infty$ | = | freestream Mach number |
| $PSP$ | = | pressure-sensitive paint |
| $Re_\infty$ | = | freestream unit Reynolds number ($m^{-1}$) |
| $SWBLI$ | = | shockwave/boundary-layer interaction |
| $\theta_{plate}$ | = | model plate angle (°) |

[1] Aerospace Technologist, Advanced Measurements and Data Systems Branch, Mail Stop 493, Senior Member AIAA.
[2] Research Technician, Advanced Measurements and Data Systems Branch, Mail Stop 493.
[3] Aerospace Technologist, Advanced Measurements and Data Systems Branch, Mail Stop 493, Senior Member AIAA.
[4] Aerospace Engineer, Aerothermodynamics Branch, Mail Stop 408A, Associate Fellow AIAA.
[5] Research Scientist, Advanced Measurements and Data Systems Branch, Mail Stop 493.
[6] Research Technician, Advanced Measurements and Data Systems Branch, Mail Stop 493.
[7] Assistant Professor, Dept. of Mechanical, Member AIAA.
[8] Professor, Dept. of Mechanical, Aerospace, & Biomedical Engineering, Fellow AIAA.
[9] Assistant Professor, Dept. of Mechanical, Aerospace, & Biomedical Engineering, Member AIAA.
[10] Graduate Research Assistant, Dept. of Mechanical, Aerospace, & Biomedical Engineering, Student Member AIAA.

# I. Introduction

This paper highlights two experimental entries performed in the 20-Inch Mach 6 Air Blowdown Tunnel at NASA Langley Research Center in collaboration with The University of Tennessee Space Institute (UTSI). The purpose of these entries was to characterize the dynamic shockwave/boundary-layer interaction (SWBLI) between a vertical cylinder on a flat plate and laminar, transitional (XSWBLI), and turbulent (SWTBLI) boundary layers with a freestream Mach number of 6 using non-intrusive optical diagnostics. Experiments performed by Murphree et al.[1,2] were among the first to specifically characterize XSWBLI induced by a vertical cylinder on a flat plate geometry using several optical measurement techniques. Recent optical studies of XSWBLI phenomenon have been performed by UTSI at Mach 2 in their low-enthalpy blow wind tunnel[3-8] and by Texas A&M University and UTSI at Mach numbers of 6 and 7 in their Adjustable Contour Expansion wind tunnel.[9] The experiments described in this paper were intended to complement previous studies by expanding the freestream unit Reynolds number range, $Re_\infty$, over which the XSWBLI phenomena has been observed. Additionally these experiments, made possible under NASA's new facility funding model under the Aeronautics Evaluation and Test Capabilities (AETC) project, promoted collaboration between university and NASA researchers.

The initial entry in the 20-Inch Mach 6 Air Tunnel at NASA Langley occurred in December of 2016. Originally, testing was to occur in November of 2016 in the 31-Inch Mach 10 Air Tunnel at NASA Langley. This facility was chosen so that the XSWBLI phenomenon could be observed at much higher Mach numbers than had previously been attempted in ground test experiments. The model selected for this experiment, a 10° half-angle wedge with a sharp leading edge (described in detail in section II.B), had previously been used by Danehy et al. [10] for boundary layer transition studies using the nitric oxide planar laser-induced fluorescence (NO PLIF) flow visualization technique. In that work, it was determined that transition could be induced downstream of a single $h_{trip}$ = 1-mm tall, $d_{trip}$ = 4-mm diameter cylindrical tripping element and that the streamwise location of the transition could be changed for a single $Re_\infty$ by changing the model angle-of-attack (AoA) (see Fig. A3 in Ref. [10] for more details). Based on the findings of that work, a decision was made to use the wedge model with the cylindrical tripping element to trip the boundary layer flow ahead of a cylindrical protuberance in order to achieve a XSWBLI.

Unfortunately, the 31-Inch Mach 10 facility had been taken offline for repairs in October of 2016 and a decision was made to move the test to the 20-Inch Mach 6 facility. Since the behavior of the boundary layer with the chosen model configuration had not been studied before in that facility and the available test time was limited, the entry was considered to be exploratory and was used to collect spatially-resolved and time-resolved flow and surface visualization data that would be used to inform a second entry. Test techniques included simultaneous high-speed schlieren (HSS) captured at 160 kHz and high-speed pressure sensitive paint captured at 10 kHz as well as oil flow visualization, captured at 750 Hz.

The second entry in the 20-Inch Mach 6 facility occurred in June and July of 2017. In this follow-on test, modifications to the wind tunnel model were made based on observations made during the first entry and included removing the cylindrical tripping element, increasing the size of the cylinder used to induce the SWBLI to increase the size of the interaction while simultaneously improving spatial resolution, and using a swept ramp array, similar to that described in Ref. [11], to trip the flow to turbulence. Simultaneous HSS (captured at 140 kHz, 100 kHz, and 40 kHz) and conventional IR thermography (captured at 30 Hz) imaging were performed simultaneously in this follow-on entry.

This paper is intended to serve as a summary of the work performed during these two entries, to detail lessons learned from each entry, and to highlight some of the datasets acquired. Details on the experimental setup, model configuration, and techniques used are provided. Papers providing a more rigorous analysis of data acquired during the second entry, including statistical, spectral, and modal decomposition methods, can be found in Refs. [12,13]. An entry examining XSWBLI in the 31-Inch Mach 10 Blowdown Wind Tunnel facility is currently planned for mid-to-late calendar year 2019, pending the success of facility repairs. The work performed and described in this paper and the upcoming entry in the 31-Inch Mach 10 facility at NASA Langley have been made possible by NASA's new facility funding model under the Aeronautics Evaluation and Test Capabilities (AETC) project.

# II. Experimental Setup

## A. Wind Tunnel Facility

All experiments discussed in this paper were performed in the 20-Inch Mach 6 Air Tunnel at NASA Langley Research Center. Specific details pertaining to this facility can be found in Refs. [14,15], with only a brief description of the facility provided here. For both entries, the nominal freestream unit Reynolds number was varied between

$1.8\times10^6$ m$^{-1}$ ($0.5\times10^6$ ft$^{-1}$) and $26.3\times10^6$ m$^{-1}$ ($8\times10^6$ ft$^{-1}$). The nominal stagnation pressure was varied between 0.21 MPa and 3.33 MPa and the nominal stagnation temperature was varied between 480 K and 520 K to achieve the desired $Re_\infty$ condition. For all runs, the nominal freestream Mach number was 6.

The nearly square test section is 520.7-mm (20.5-inches) wide by 508-mm (20-inches) high. Two 431.8-mm (17-inch) diameter windows made of Corning 7940, Grade 5F schlieren-quality glass serve as the side walls of the tunnel and provide optical access for the high-speed schlieren measurements. A rectangular window made of the same material as the side windows served as the top wall of the test section and provided optical access for the high-speed PSP and oil flow measurements. For the second entry, this top window was replaced with a Zinc Selenide (ZnSe) window with an anti-reflection coating capable of passing IR wavelengths between 8μm and 12μm with greater than 98% transmittance.

The model was sting supported by a strut attached to a hydraulic system that allows for the model pitch angle to be adjusted between -5° to +55°. For the first entry, an initial pitch/pause sweep of the model AoA was performed to observe the resulting SWBLI. Ultimately, however, the sting pitch angle for this entry was fixed at +10.0° so that the angle of the top surface of the wedge relative to the streamwise axis of the tunnel (referred to herein as the *plate angle*, $\theta_{plate}$), was $\theta_{plate}$ = 0°. For the second entry, $\theta_{plate}$ = 0° and $\theta_{plate}$ = -13.25° were initially tested with the swept ramp array (discussed in the following section) to determine which orientation produced conditions most favorable for XSWBLI to occur based on the heating signatures observed over the top surface of the model in the IR thermography images. Based on these initial tests, $\theta_{plate}$ = -13.25° was set for the remainder of the runs in the second entry.

For both entries, any model changes were performed in a housing located beneath the closed test section. Prior to performing a run of the tunnel, the housing was sealed and the tunnel started. Once the appropriate freestream conditions were achieved, the model was injected into the test section using a hydraulic injection system.

## B. Model Geometry

For all runs, a 10° half-angle (20° full-angle) wedge model with a sharp leading edge was used. The model is described in detail in Refs. [10,16]. The top surface of the sharp leading edge of the model extended 47.8 mm from its upstream-most edge to a junction with the upstream edge of a stainless steel top plate that then extended an

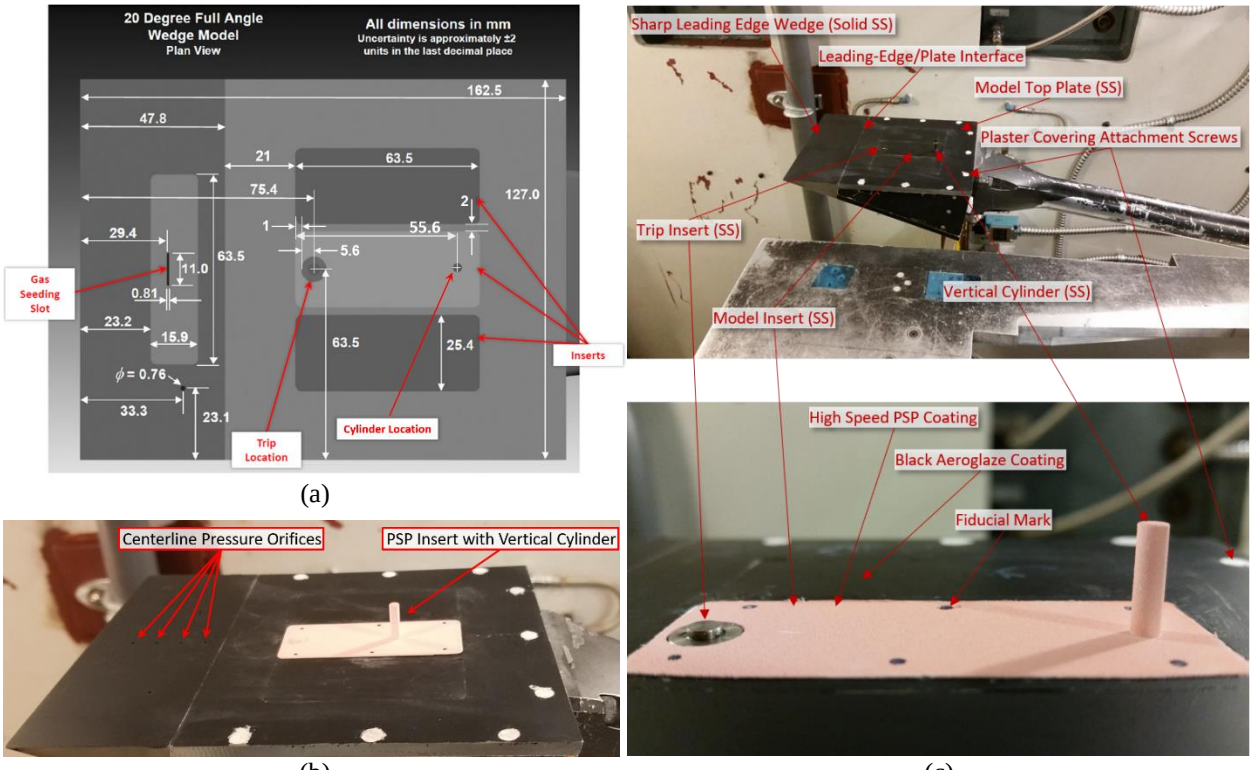


**Fig. 1 (a) Schematic of top surface of wedge model with gas seeding insert, (b) perspective view of the model in the 20-Inch Mach 6 tunnel with centerline pressure orifices on sharp leading edge, and (c) a perspective view of the model with stainless steel (top) and SLA middle insert (bottom) during the first entry. Flow occurs from left to right.**

additional 114.7 mm to the end of the model. The entire top surface of this wedge model (including the sharp leading edge and top plate) was essentially a flat plate that was 127.0-mm (5-inches) wide and 162.5-mm (6.4-inchs) long. A schematic of the top surface of the model in provided in Fig. 1a. For all runs, the top surface of the model was painted with a black high-temperature paint. The sharp leading edge shown in Fig. 1a (along with the gas seeding slot) was used only used for the second entry. A different sharp leading edge, shown in Fig. 1b and described in the next section, was used for the first entry.

The top plate (127.0-mm wide by 114.7-mm long) accommodated three rectangular stainless steel inserts (denoted as inserts in Fig. 1a) with rounded corners that measured 25.4-mm wide by 63.5-mm long, with the leading edge of each insert located 68.8-mm downstream of the leading edge. The middle insert (denoted as model insert in Fig. 1c) was centered on the spanwise axis of symmetry of the model and accommodated the vertical cylinders used to induce the SWBLIs. The middle insert was also painted with a flat black paint when high-speed PSP measurements were not being performed. The two side inserts were spaced 2 mm from the spanwise edges of the middle insert. The top surfaces of these inserts were also flush with the rest of the plate. These side inserts were painted with a high-temperature black paint for all runs. A fast response K-type thermocouple (Omega, SA1XL-K-SRTC) was placed on the underside of each side insert to monitor plate temperature over the course of each wind tunnel run.

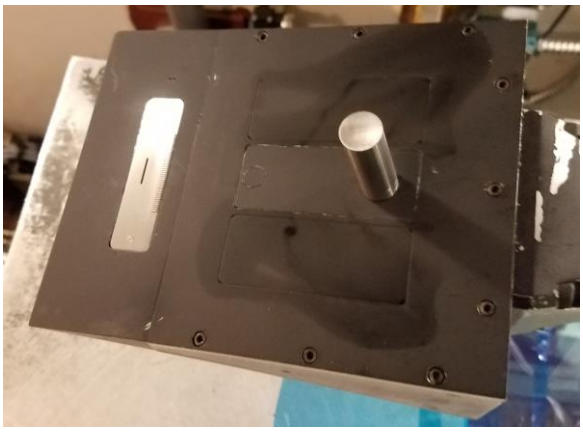

(a)

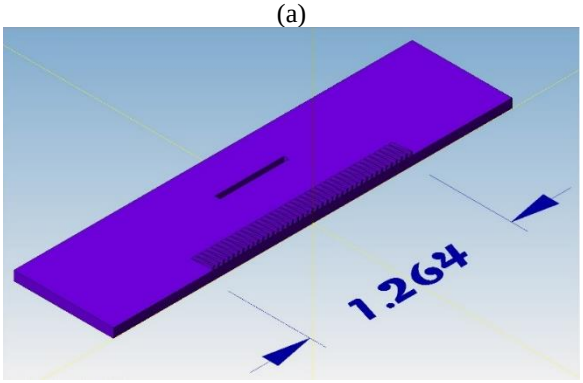


(b)

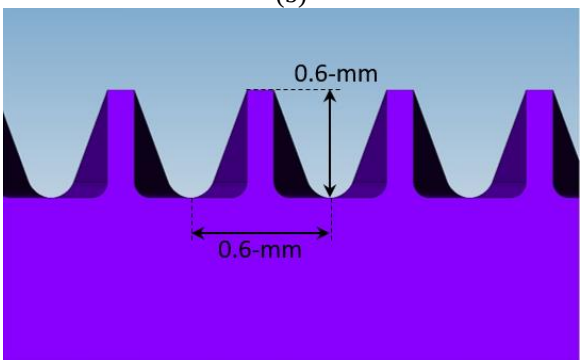


(c)

**Fig. 2 (a) Perspective view of the wedge model with swept ramp array insert and the $d_{cylinder}$ = 12.7 mm, $h_{cylinder}$ = 38.1 mm vertical stainless steel cylinder used in the second entry. A perspective (b) and upstream-facing view (c) of the swept ramp array insert with dimensions given in inches and mm, respectively.**

*1. First Entry Model Configuration*

For the first entry, the stainless steel sharp leading edge mounted on the wedge model and shown in Fig. 1b had a series of four 1-mm-diameter pressure orifices spaced 8.5-mm apart with the first orifice being 15.5-mm from the leading edge. All were aligned to the model's spanwise axis of symmetry and were used to monitor the plate pressure and strength of the viscous interaction near the leading edge. This wedge replaced the leading edge wedge that accommodated a gas seeding insert with a seeding slot, as shown in Fig. 1a. Two different cylindrical tripping inserts could be mounted to the middle insert for this test at the trip location shown in Fig. 1a and denoted as trip insert in Fig. 1c. The first of these inserts had a top surface that was flush with the rest of the middle insert's top surface and the rest of the top plate. The second insert had a $d_{trip}$ = 4 mm diameter, $h_{trip}$ = 1.0 mm tall cylindrical protuberance that was used to trip the boundary layer. A $d_{cylinder}$ = 3.175 mm diameter, $h_{cylinder}$ = 12.7 mm tall vertical cylinder was mounted on the middle insert downstream of the trip location, located 55.6-mm downstream of the leading edge of the middle insert (denoted as vertical cylinder in Fig. 1c). This vertical cylinder was used to generate the SWBLI.

*2. Second Entry Model Configuration*

For the second entry, the leading edge wedge shown in Fig. 1a was mounted to the model. For a portion of the runs, the seeding insert shown in Fig. 1a was mounted to the leading edge wedge and had a top surface that was flush with the rest of the model's top surface. This gas seeding slot was not used for any of the runs and was covered by a thin piece of Kapton® tape. For another portion of the runs, a second insert that had a series of 41 swept ramps positioned side-by-

side with a base width of 0.6 mm, an end width of 0.15 mm, a total length of 3.4 mm, and an end height of 0.6 mm was used to generate streamwise vorticity and trip the boundary layer to turbulence. This array is shown mounted to the sharp leading edge in Fig. 2a, with a CAD perspective view and upstream-facing view shown in Fig. 2b and Fig. 2c, respectively. The base of this swept ramp array was positioned 12.5-mm downstream of the leading edge of the insert. This swept ramp was designed based on work described in Ref. [11], with the height of the ramps sized to be approximately the height of the boundary layer thickness at that particular streamwise location. A $d_{cylinder}$ = 12.7-mm diameter, $h_{cylinder}$ = 38.1-mm tall vertical cylinder was mounted to the middle insert with its center located 55.6-mm downstream of the leading edge of the middle insert (shown in Fig. 2a). This larger vertical cylinder was used to generate a larger SWBLI region relative to that observed in the first entry.

### C. Optical Diagnostics

*1. First Entry*

During the first entry, HSS imaging was performed using a Z-type configuration with two 16-inch diameter, 8-foot focal length mirrors. A light source consisting of a green Luminus CBT-120-G LED driven by a PicoLAS LDP-240-100V3 laser diode driver provided pulsed illumination at a rate of 160 kHz with a 200 ns pulse width. The light source was fitted with a 1:1 achromat lens pair (Thorlabs MAP104040-A) that was positioned over the LED's light-emitting surface such that it was re-imaged onto an adjustable graduated aperture. This allowed for adjustment of the size of the point source imaged by the schlieren system, which was set to approximately 2.5 mm for the first entry. Beyond the aperture, a shortpass filter (Thorlabs FESH0550) was used to block LED emission beyond 550 nm to avoid interference with the high-speed PSP signal. The light source design was based in part on the design by Willert et al. [17,18]. A Photron SA-Z 2100K monochromatic camera captured the schlieren images at a framing rate of 160 kHz using a 180-mm focal length lens (Nikon AF Nikkor 180 mm f/2.8D). A green pass-band filter (Edmund Optics 89-790) was place in front of the imaging lens to block scattered light from the PSP illumination sources and emission from the PSP while passing the green pulsed LED light. The camera was mounted such that the top and bottom edges of the camera pixels were roughly aligned with the model surface.

High-speed PSP imaging was performed using three ISSI LM2XX-400 400 nm illumination sources. Images were captured at a framing rate of 10 kHz using a Photron AX-200 camera fitted with a 105-mm focal length lens (Nikon AF DC-Nikkor 105 mm f/2D) that was mounted on the top of the wind tunnel. A bandpass filter centered on 650 nm with a 40 nm full-width at half-maximum transmission width was placed on the front of the camera's lens to limit the wavelength range captured by the PSP camera. This is the first time that high-speed PSP measurements have been performed in the 20-Inch Mach 6 Air Blowdown Tunnel at NASA Langley Research Center.

Three oil flow visualization runs were performed using the same Photron AX-200 camera and 105-mm focal length lens combination as was used for the high-speed PSP imaging as well as the same three ISSI LM2XX-400 400 nm LED illumination sources, all mounted to the top of the wind tunnel. However, the 650 nm bandpass filter was replaced with a 515 nm long pass filter. This filter blocked scatter from the 400 nm LEDs but passed emission from the green Day-Glo phosphorescent powder mixed in with the 200 weight oil. For the oil flow visualization, images were only acquired at a rate of 750 Hz.

In the first entry, triggering of the HSS, high-speed PSP, and oil-flow cameras was controlled by a Berkeley Nucleonics Model 577 digital delay/pulse generator.

*2. Second Entry*

For the second entry, a lens-based HSS system consisting of two 1-m focal length, 152.4-mm diameter achromat lenses was used to image the flow. The same LED illumination source, Photron SA-Z 2100K monochromatic camera and 180-mm focal length lens were used to capture images at framing rates of 40 kHz, 100 kHz, and 140 kHz with a 200 ns LED pulse width all during a single run of the tunnel. The different framing rates captured within a single run allowed for a large (896×576 pixels), moderate (1024×184 pixels), and small (1024×120 pixels) field-of-view of the model and flowfield to be imaged. As in the first entry, the camera was mounted such that the top and bottom edges of the camera pixels were roughly aligned with the model surface. For this entry, the HSS camera was internally triggered and controlled via the Photron PFV software. The pulsed LED light source was triggered by a trigger signal provided by the camera, allowing for the field-of-view and framing rate of the HSS system to be quickly changed during a run of the wind tunnel.

Long-wave infrared (LWIR) imaging of the top surface of the wind tunnel model was also performed in order to identify regions of increased heating corresponding to boundary layer transition and points affected by the SWBLI. The LWIR images were captured at a frame rate of 60 Hz using a FLIR ThermaCAM SC3000 IR camera. This LWIR camera was not externally triggered by the HSS camera or other source and therefore was not synchronized with the HSS system. The camera had a spectral range of 8 μm to 9 μm and was mounted on top of the wind tunnel.

## III. Results

### A. First Entry

*1. Summary of Results*

Fig. **3** shows eight sample single-shot schlieren images taken from high-speed schlieren image sequences from the first entry in the 20-Inch Mach 6 Air Tunnel. Flow is from left to right in these figures. Prior to each run of the tunnel a sequence of tunnel-off images were acquired, averaged together, and subtracted from the full tunnel-on image sequence to minimize image artifacts such as window markings, scratches, and defects. Figures 2a, 2b, 2c, and 2e show resulting sample single-shot base flow (no trip, no cylinder), flow with no cylinder, flow with no trip, and flow with trip and cylinder images acquired during the first entry. The base flow condition for this entry was chosen to be $Re_\infty \approx 22.6\times10^6\ m^{-1}$. The remaining images show the flow with the trip and cylinder mounted on the model for $Re_\infty$ ranging from approximately $26.3\times10^6\ m^{-1}$ to $13.1\times10^6\ m^{-1}$.

In these single-shot images, the oblique shock emanating from the sharp leading edge is clearly visible, as are three distinct oblique shock features farther downstream (most visible in Fig. 3a). The most upstream feature behind the leading edge oblique shock is thought to have originated from or near small steps located between the leading edge and top plate junction. The other two features most likely originated from small steps either at the junction between the top plate inserts and the top plate or from the attachment screw holes located around the periphery of the top plate.

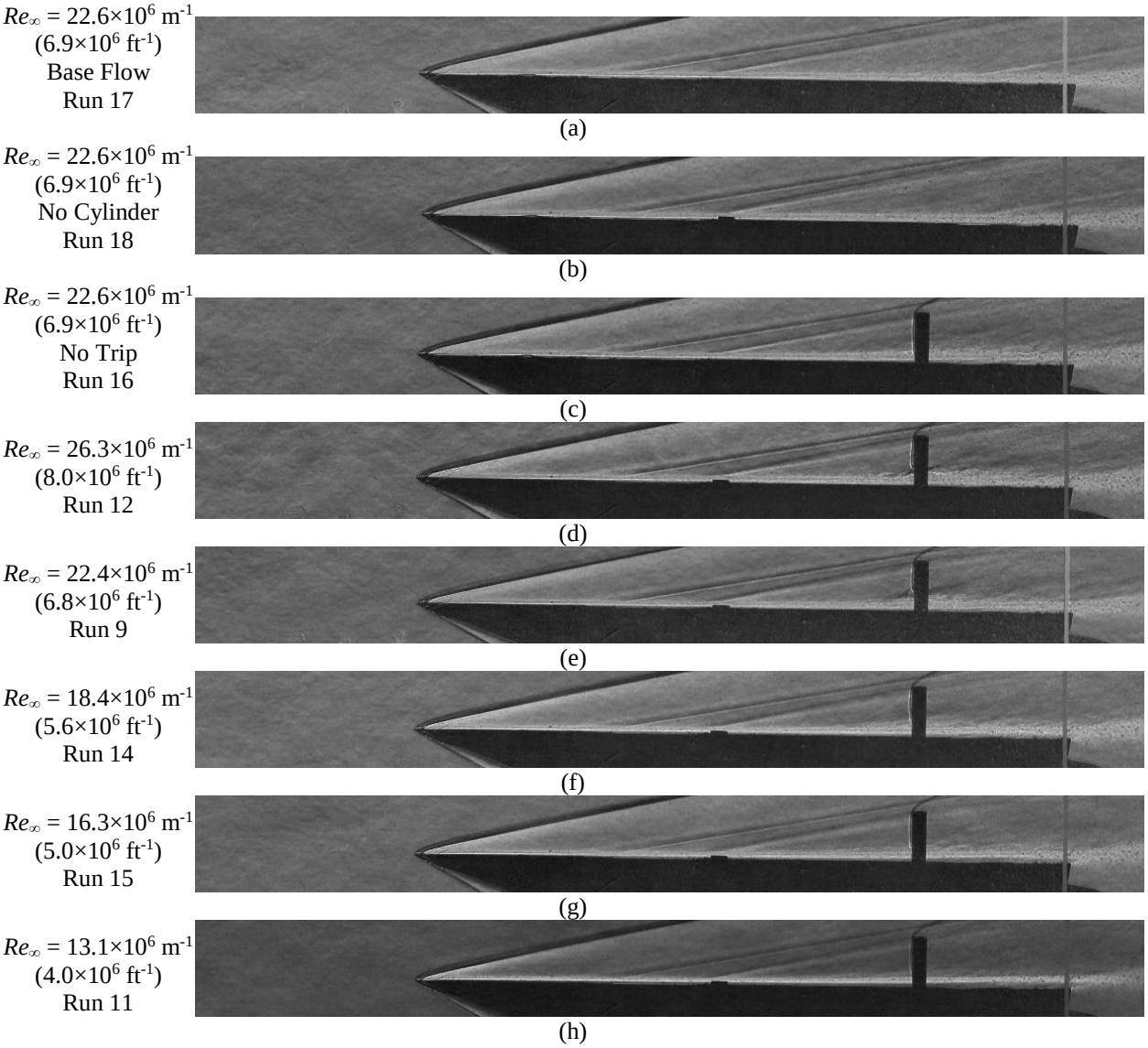


**Fig. 3 Single-shot sample schlieren images from first entry.**

When viewing an image sequence of the model without and with the cylindrical tripping element (corresponding to Fig. 3a and Fig. 3b, respectively), there is no visible difference between the time-resolved flowfields downstream of the tripping element location. When viewing the image sequence corresponding to the model configuration with the vertical cylinder but no trip at the same condition as the base flow ($Re_\infty = 22.6\times10^6$ m$^{-1}$ in Fig. 3c), a small level of unsteadiness around the base of the vertical cylinder is observed. When viewing the image sequences with both the cylindrical tripping element and vertical cylinder present, a larger degree of unsteadiness – relative to the condition in Fig. 3c – is observed ahead of the vertical cylinder, with the level of unsteadiness decreasing with decreasing $Re_\infty$. These observations indicate that the combination of the cylindrical tripping element and vertical cylinder produced a higher degree of unsteadiness in the SWBLI than if the vertical cylinder alone had been used.

Fig. 4 better demonstrates this point as it shows both the time-average (left) and standard deviation (right) of the first one-thousand single-shot images. The order of these images corresponds to the same order as the single-shot images shown in Fig. 3, from top to bottom. The intensity bounds for the time-average images have been kept constant, as have the intensity bounds for the standard deviation images, which are shown in false color. Note that each of these images has been rotated by 0.9° in the counter-clockwise direction to account for a slight misalignment between the camera and model surface. When comparing the standard deviation images without and with the cylindrical tripping element for nearly the same $Re_\infty$ (Fig. 4c and Fig. 4e, respectively), a higher degree of unsteadiness, characterized by the higher intensity region centered at approximately ⅓ $h_{cylinder}$ just ahead of the vertical cylinder, is observed. For the highest $Re_\infty$ condition with both the cylindrical tripping element and vertical cylinder, the greatest level of unsteadiness is observed and is centered at ⅓ $h_{cylinder}$ just ahead of the vertical cylinder (standard deviation image in Fig. 4d). As $Re_\infty$ is decreased, the level of unsteadiness decreases and what appears to be the signature of the front foot of a λ-shock feature diminishes. The signature of the front foot of a λ-shock feature is most apparent in the time-average images in Fig. 4d.

Fig. 5 shows four sample 10-shot time-average (upper figures) and standard deviation (lower figures) PSP images taken from high-speed PSP image sequences during the first entry. Each image sequence has been processed to minimize the apparent motion between the wind tunnel model and camera during the run using the ImageJ-based[19] routine, *Image Stabilizer*.[20] Flow in these images is from left to right. Fig. 5a, 5b, 5c, and 5d correspond to the conditions at which the single-shot schlieren images were acquired in Fig. 3a, 3b, 3c, and 3e, respectively. It should be noted that these images do not strictly relate to the surface pressure field, as the surface temperature field has some level of influence on the emission characteristics of the high-speed PSP.

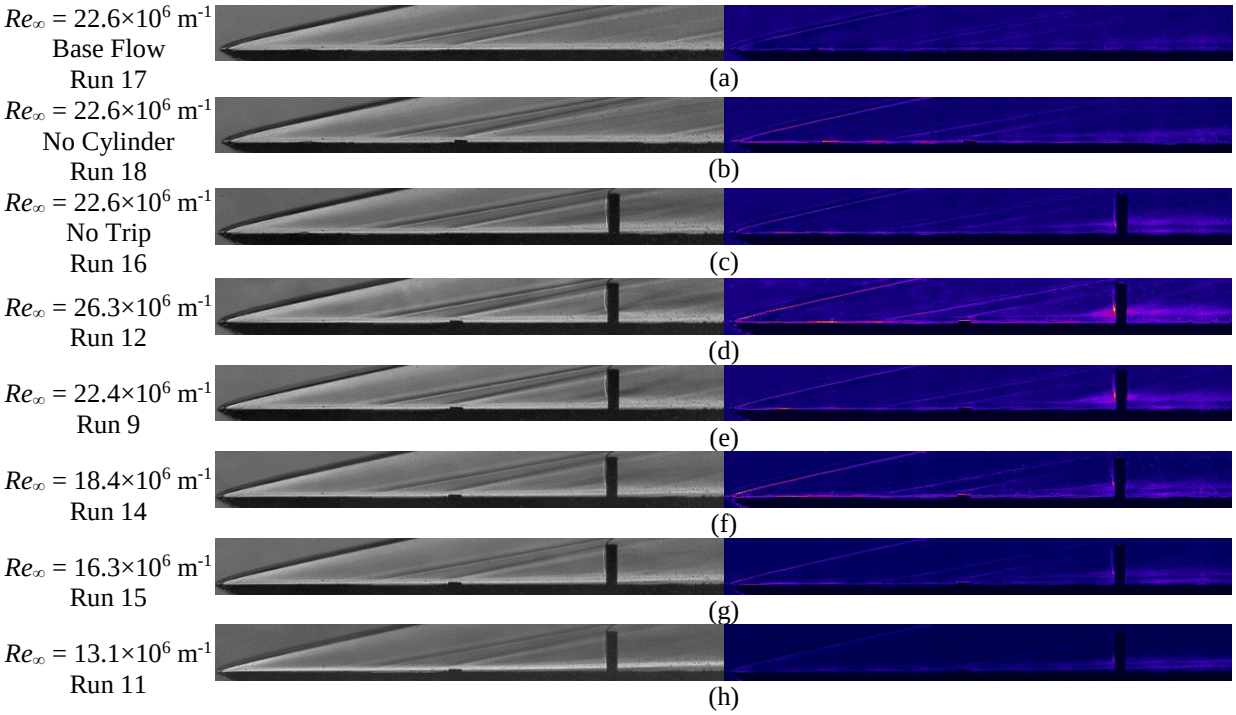


**Fig. 4 Time-average (left) and standard deviation (right) of SWBLI flowfield in false color. Images correspond to conditions of single-shot images shown in Fig. 3, from top to bottom.**

In Fig. 5a1, no noticeable pressure gradients are observed over the middle insert, which corresponds to the base flow case. Pressure fluctuations are also not apparent in the standard deviation image in Fig. 5a2 for the same condition. With the cylindrical tripping element in place (but no vertical cylinder), streamwise streaks are observed emanating from the upstream edge of the element in Fig. 5b1. This behavior is consistent with PSP images acquired with the same model in the 31-Inch Mach 10 facility at Langley in Ref. [16] (albeit at different freestream conditions). A secondary region of varying pressure is also observed near the rear, starboard side of the middle insert. It is unclear what specifically caused this variation, as it is not observed in any of the other PSP images. A low level of unsteadiness is observed for this case, as shown in the standard deviation image of Fig. 5b2. Without the cylindrical tripping present, a horseshoe vortex type structure is observed to form ahead of the vertical cylinder in the SWBLI region, as shown in Fig. 5c1. As this structure wraps around the vertical cylinder, the two visible ends of the structure at the downstream-most edge of the middle insert appear to bifurcate. Note that a region of slightly increased pressure (light blue region) ahead of the more complex and higher pressure structure immediately just in front of the vertical cylinder can be seen. A higher degree of unsteadiness is observed for this configuration, with distinct outlines of unsteady regions apparent in Fig. 5c2. In Fig. 5d1, the streamwise vortices that proceed from the cylindrical tripping element appear to have a strong influence on the structure of the SWBLI region ahead of the vertical cylinder. Two regions of increased pressure proceed upstream of the SWBLI region and are aligned with the streamwise vortices generated by the cylindrical tripping element. In this configuration, the bifurcation observed without the cylindrical tripping element present is not

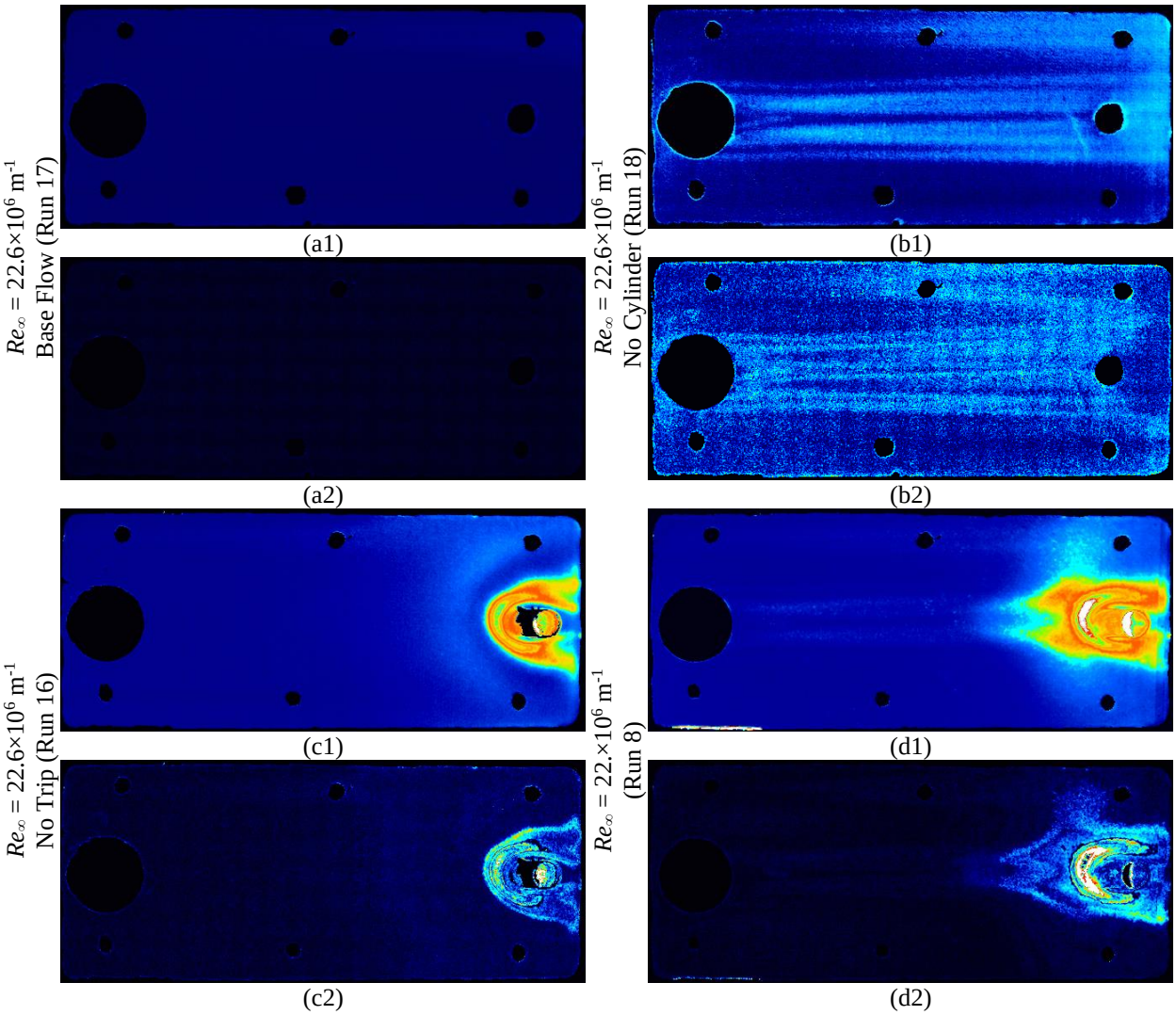


**Fig. 5 10-shot time-average (upper) and standard deviation (lower) sample PSP images from first entry. A false color table has been applied to the images.**

observed. The region of increased pressure ahead of the higher pressure structure observed in Fig. 5c1 is also absent. Again, a significant level of unsteadiness, highlighted in Fig. 5d2, is observed.

Fig. 6a shows the wedge model in the tunnel with the Day-Glo phosphorescent powder on 200 weight oil under 400 nm UV illumination. Fig. 6b show a single-shot image of the model several seconds into a run at $Re_\infty = 22.7\times10^6$ $m^{-1}$ with only the cylindrical tripping element (denoted by the red circle). The edges of the middle insert are denoted by the yellow outline. Flow is from left to right. Streaks are observed wrapping around the trip and proceeding downstream in a manner similar to that observed in the time-average PSP image in Fig. 5b1, although the influence of the tripping element appears to extend farther in the spanwise direction in the oil flow images than it does in the PSP images. Fig. 6c and 6d were for runs with both the cylindrical tripping element (again, denoted by the red circle) and vertical cylinder (denoted by the red cylinder) at the same nominal $Re_\infty$ as in Fig. 6b. In these images, streaks are again observed wrapping around the trip and proceeding downstream towards the vertical cylinder. A relatively large recirculation/reversed-flow region ahead of the vertical cylinder, and near the port spanwise edge of the middle insert, is observed. A slightly smaller recirculation/reversed-flow region is also observed on the starboard side in these

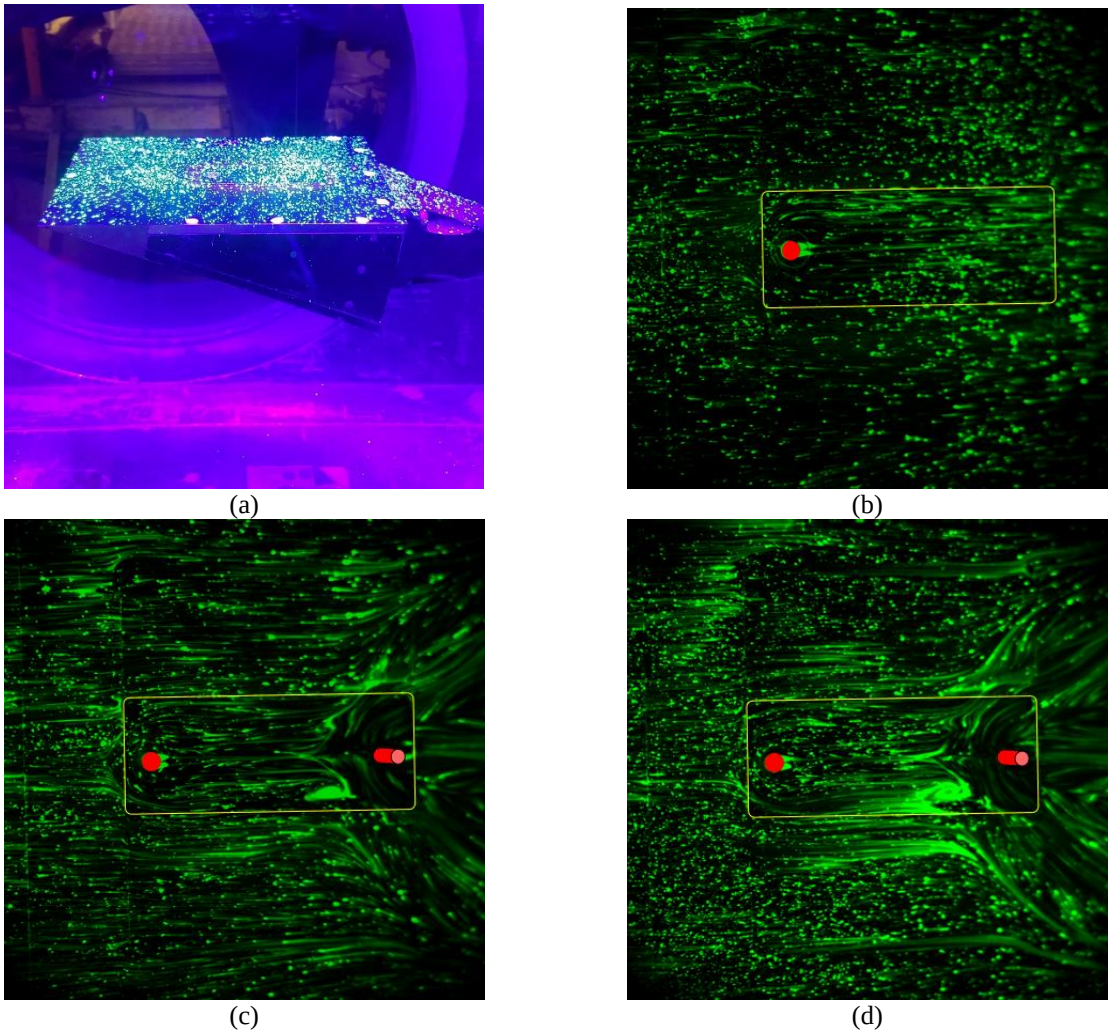


**Fig. 6 (a) Wedge model with Day-Glo phosphorescent powder on 200 weight oil in 20-Inch Mach 6 test section under 400 nm UV illumination. Single-shot oil flow images taken several seconds into the run with (b) cylindrical tripping element only at $Re_\infty = 22.7\times10^6$ $m^{-1}$ (Run 19), (c) cylindrical tripping element and vertical cylinder at $Re_\infty = 22.6\times10^6$ $m^{-1}$ (Run 20), and (d) an additional run with the cylindrical tripping element and vertical cylinder at $Re_\infty = 22.5\times10^6$ $m^{-1}$ (Run 21). Flow is from left to right and a false color table has been applied to (b), (c), and (d). The red circles indicate the position of the cylindrical tripping element. The red cylinder represents the position of the vertical cylinder. The yellow box in (b), (c), and (d) corresponds to the edges of the middle insert.**

figures. These regions appear to occur upstream and to the outer spanwise edge of the two regions of increased pressure ahead of the vertical cylinder observed in the PSP in Fig. 5d1. In both Fig. 6c and Fig. 6d, the spanwise influence of the vertical cylinder grows rapidly as flow proceeds around it and continues downstream.

*2. Lessons Learned in the First Entry*

Several issues that adversely affected data acquisition were identified after the first entry and are described here. A second entry was planned soon after the first entry so that these issues could be addressed. The most apparent issue with the first entry was that the size of the SWBLI was not sufficient to be adequately resolved by the HSS system in the 20-Inch Mach 6 facility. Additionally, since schlieren is a path-averaged flow visualization technique, the wall-normal density gradients associated with the boundary layer flow over the top surface of the wedge model obscured the view of the SWBLI. This was especially true near the junction between the model surface and leading edge of the vertical cylinder, where the λ-shock and upstream influence structures associated with the SWBLI occur. Originally, the selection of the vertical cylinder dimensions ($d_{cylinder}$ = 3.175 mm, $h_{cylinder}$ = 12.7 mm) was made so that they matched those of the vertical cylinder used in experiments at UTSI (see Ref. [13]). However, after the first entry it was apparent that a larger cylinder would be needed to properly resolve the SWBLI. Therefore, for the second entry, a $d_{cylinder}$ = 12.7 mm, $h_{cylinder}$ = 38.1 mm vertical cylinder was fabricated. The dimensions of this new cylinder were selected based on recommendations by Leidy et al. [9], which were based on observations by Dolling and Bogdonof [21],that a ratio of $h_{cylinder}$ / $d_{cylinder}$ ≥ 2.4 will ensure a well-developed λ-shock structure. Additionally, the $d_{cylinder}$ dimension was chosen based on experimental data of a cylinder-wedge hypersonic flow detailed in Ref. [22] where the stand-off distance of the shock, $\Delta_{shock}$, can be approximated by:

$$\frac{\Delta_{shock}}{d_{cylinder}} = 0.386 \cdot exp^{\left(\frac{4.67}{M_\infty}\right)} \qquad \text{Eq. 1}$$

For the first entry, $\Delta_{shock}$ was on the order of 0.6-0.8 mm and it was difficult to distinguish this shock from the leading edge of the cylinder, as the HSS system resolution was not sufficient. A decision was made to triple the diameter of the cylinder the stand-off shock associated with the SWBLI so that this shock could be clearly distinguished from the leading edge of the vertical cylinder. Additionally, it was decided that in order to improve the spatial resolution of the HSS measurements, and therefore better resolve the SWBLI region, a lens-based schlieren system would be used in the second entry.

Based on the high-speed PSP and HSS image sequences, it was decided that the cylindrical tripping element would be removed for the second entry, as it was difficult to determine if the state of the boundary layer approaching the vertical cylinder was ever truly transitional for observation of XSWBLI. Additionally, the non-uniformity of the flow approaching the vertical cylinder generated by the single cylindrical tripping element was undesirable, as it restricted interpretation of the results. In the first entry, the flow approaching the vertical cylinder and the SWBLI region consisted of a streamwise streaks confined to a narrow spanwise region downstream of the trip. For the second entry, it was decided that either no tripping element would be used or a tripping element that generated a more uniform (with respect to the spanwise dimension) inflow condition to the SWBLI region, such as the swept ramp array, would be used.

Finally, it was determined that IR thermography should be employed in the second entry to better determine when and where transition-to-turbulence occurred.

## B. Second Entry

*1. Summary of Results*

Fig. 7 shows HSS single-shot, time-average, and standard deviation images from left to right acquired during the second entry. HSS data acquired with the swept ramp array mounted in the gas seeding slot insert location, shown in Fig. 1a, and the $d_{cylinder}$ = 12.7 mm, $h_{cylinder}$ = 38.1 mm vertical cylinder centered 55.6 mm downstream of the leading edge of the middle insert is shown in the top half of Fig. 7. HSS data acquired with no tripping element mounted on the model with the vertical cylinder is shown in the lower half of Fig. 7. Flow in all images is from left to right.

In general, for both the swept ramp array and no-trip model configurations, the signature of the SWBLI structure becomes more pronounced with increasing $Re_\infty$. Additionally, the presence of the upstream influence shock, which extends ahead of the front foot λ-shock structure, becomes more apparent as $Re_\infty$ is increased. For both configurations, as $Re_\infty$ increased, the level of unsteadiness in the approaching boundary layer increases. This is most apparent in the single-shot and standard deviation images in Fig. 7. Additionally, the standard deviation images show that as $Re_\infty$ is increased, the SWBLI structure evolves until no significant differences can be observed, indicative of the onset of a SWTBLI. At both the low and high ends of the $Re_\infty$ range, the SWBLI structures in all three image types (single-shot,

time-average, and standard deviation) for the model configuration with and without the swept ramp array look nearly identical. In all images, weak shock waves can be observed that are most likely attributed to small steps in located at several locations on the top plate surface, and not necessarily on the model's spanwise axis of symmetry. These waves most likely had little to no influence on the SWBLI.

It is only at the moderate $Re_\infty$ conditions that small differences between the two configurations can be seen. For instance, close inspection of the time-average image at $Re_\infty = 9.5\times10^6$ m$^{-1}$ for the swept ramp array configuration shows that the density gradient across the forward foot of the λ-shock structure is stronger than it is for the no-trip configuration at the same nominal $Re_\infty$. Additionally, small differences between the tripped and no-trip configuration are observed in the region ahead of the vertical cylinder just below the shock-shock interaction caused by the leading edge oblique shock and stand-off shock. For the tripped configuration, the stand-off shock just below the shock-shock interaction but above the SWBLI region is nearly vertical for $Re_\infty \geq 7.9\times10^6$ m$^{-1}$ and appears to indicate that the SWBLI does not extend as high for the tripped configuration as it does for the no-trip configuration. A more in-depth analysis

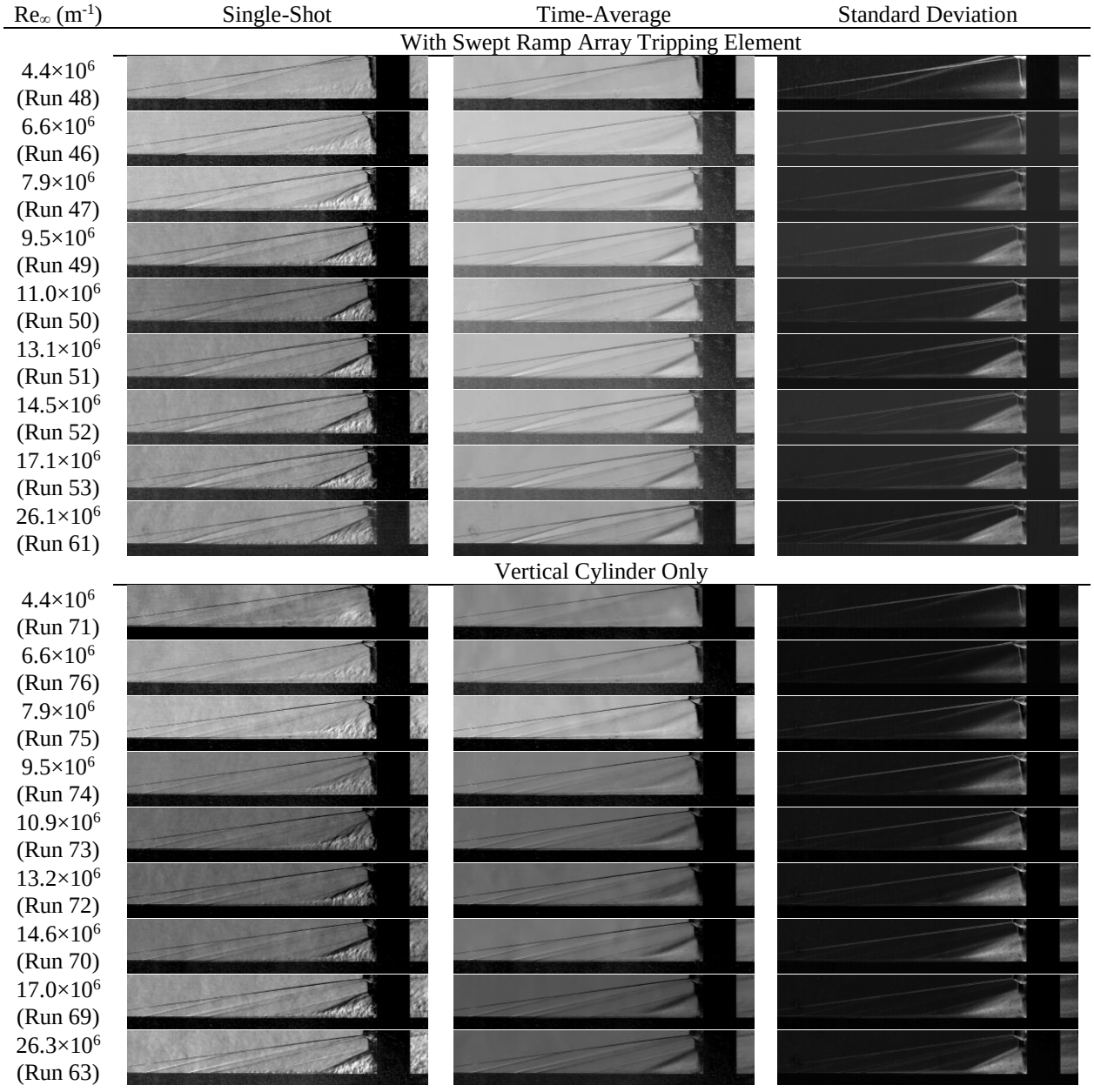


**Fig. 7 Single-shot, time-average, and standard deviation schlieren images from high-speed schlieren image sequences with (top) and without (bottom) swept ramp array tripping element.**

of the no-trip configuration HSS data, including the application of spectral and modal decomposition analysis methods, is provided in Refs. [12,13].

Fig. 8 shows single-shot IR thermography images obtained during the second entry. As in Fig. 7, the top portion of the figure shows results with the swept ramp array configuration and the lower portion of the figure shows results with the no trip configuration. In all images flow is from left to right and a false color table has been applied.

In general, many of the IR characteristics across the top surface of the wedge model are similar for both the tripped and no-trip configurations. In all images, an increased line of heating is observed at the leading edge of the model. Increased heating on the two side inserts on the top plate is also observed for all runs, which is attributed to the decreased thickness of the insert relative to the middle insert and the rest of the top plate. As $Re_\infty$ is increased, a region of increased heating that extends ahead of the vertical cylinder in a large arc becomes more pronounced. Additionally, increased heating regions emanating diagonally downstream from the vertical cylinder are observed for all runs, with their magnitude increasing with increasing $Re_\infty$.

For the tripped configuration in the top half of Fig. 8, a region of increased heating immediately behind, and that spans the width of, the swept ramp array becomes more pronounced with increasing $Re_\infty$. This phenomenon is not observed in the IR data corresponding to the no-trip configuration. At the highest $Re_\infty$ condition for the tripped configuration, additional increased heating signatures corresponding to turbulent wedge structures can also be observed at various locations on the model away from the downstream projection of the swept ramp array. Interestingly for the no-trip configuration, increased heating signatures from turbulent wedge structures at several locations on the top of the model surface can be observed for $Re_\infty \geq 13.2\times10^6$ m$^{-1}$. A more in-depth analysis of the no-trip configuration IR thermography data is provided in Refs. [12,13].

*2. Lessons Learned in the Second Entry*

Perhaps the most obvious issue that occurred during the second entry as well as with the first entry was the visualization of shocks that most likely originated from small steps that existed at several locations across the top surface of the model. Care was taken before every run and after every model configuration change to minimize the size of these steps and create as smooth a top surface as possible. The model selected for these tests was originally constructed to be versatile and allow for numerous leading edge wedge, top surface, and insert geometries to be mounted on it. Unfortunately, this versatility comes at the cost of not having a smooth surface over which to perform a test, as assembly of the various inserts and components will inevitably lead to small surface irregularities. Additionally, the varying thicknesses of the different inserts resulted in irregular heating patterns over the three inserts on the top plate. For the 31-Inch Mach 10 test, a single flat plate model will be used study the SWBLI phenomenon.

## IV. Conclusions

This paper summarizes two entries in the 20-Inch Mach 6 Air Blowdown tunnel at NASA Langley Research Center performed in collaboration with the University of Tennessee Space Institute to study the shockwave/boundary-layer interaction that occurs between a vertical cylindrical protuberances on a flat plate with laminar, transitional, and turbulent hypersonic boundary layer conditions. Several optical diagnostics including high-speed schlieren, high-speed pressure-sensitive paint, oil flow visualization, and IR thermography were used to study this phenomenon. After the first entry, several of the lessons learned were used to inform a second entry in the facility that occurred approximately 6 months later. Lessons learned in both entries will be used to guide test planning for a future entry in the NASA Langley 31-Inch Mach 10 facility that will also study the shockwave/boundary-layer interaction phenomenon generated by a vertical cylinder on a flat plate.

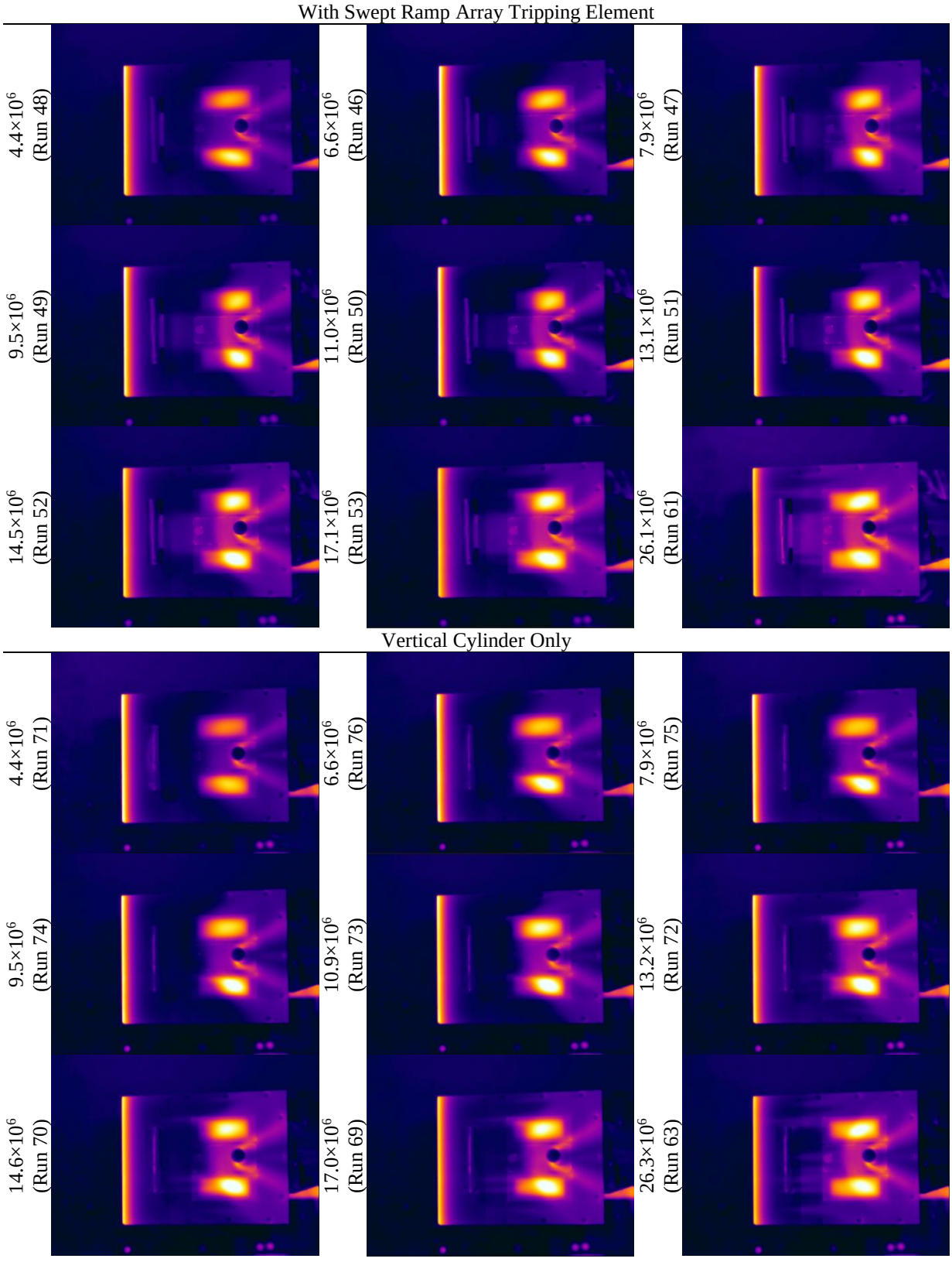


**Fig. 8 IR Thermography single-shot images with (top) and without (bottom) swept ramp array element.**

## Acknowledgments

The authors would like to thank Mark Kulick at NASA LaRC for his assistance with model fabrication. Wayne Page, Josh Weisberger, Kevin Hollingsworth, Sheila Wright, Johnny Ellis, Grace Gleason, Larson Stacy, Jonathan Crider, and Matt Rhode at NASA Langley are acknowledged for their assistance with test setup, execution, and support. Support for wind tunnel testing at NASA Langley Research Center was provided by the Hypersonic Technology Project (HTP), Transformational Tools and Technologies (TTT) project, and the Aeronautics Evaluation and Test Capabilities (AETC) project. Authors from The University of Tennessee Space Institute would like to acknowledge support from the U. S. Office of Naval Research under award number N00014-15-1-2269

## References

[1] Murphree, Z. R., Jagodzinski, J., Hood, E.S., Clemens, N.T., and Dolling, D.S., "Experimental Studies of Transitional Boundary Layer Shock Wave Interactions," 44th AIAA Aerospace Sciences Meeting and Exhibit, AIAA Paper 2006-326, Reno, NV, January 9-12, 2006.

[2] Murphree, Z. R., Yuceil, K.B., Clemens, N.T., and Dolling, D.S., "Experimental Studies of Transitional Boundary Layer Shock Wave Interactions," 45th AIAA Aerospace Sciences Meeting and Exhibit, AIAA Paper 2007-1139, Reno, NV, January 8-11, 2007.

[3] Lash, E.L., Combs, C.S., Schmisseur, J.D., Kreth, P.A., and Beckman, E.A., "Developing an Image-Based Analysis of the Dynamics of Transitional Shock Wave-Boundary Layer Interactions," 32nd AIAA Aerodynamic Measurement Technology and Ground Testing Conference, AIAA Paper 2016-4320, Washington, D.C., June 13-17, 2016.

[4] Combs, C.S., Lash, E.L., and Schmisseur, J.D., "Investigation of a Cylinder-Induced Transitional Shock Wave-Boundary Layer Interaction using Laser Diagnostics," 32nd AIAA Aerodynamic Measurement Technology and Ground Testing Conference, AIAA Paper 2016-4321, Washington, D.C., June 13-17, 2016.

[5] Lash, E.L., Combs, C.S., Kreth, P.A., and Schmisseur, J.D., "Experimental Investigation of a Cylinder-Induced Transitional Shock Wave-Boundary Layer Interaction," 55th AIAA Aerospace Sciences Meeting, AIAA Paper 2017-760, Grapevine, TX, January 9-13, 2017.

[6] Lash, E.L., Combs, C.S., Kreth, P.A., and Schmisseur, J.D., "Study of the Dynamics of Transitional Shock Wave-Boundary Layer Interactions using Optical Diagnostics," 47th AIAA Fluid Dynamics Conference, AIAA Paper 2017-3123, Denver, CO, June 5-9, 2017.

[7] Combs, C.S., Lindörfer, S.A., Kreth, P.A., and Schmisseur, J.D., "The Role of Boundary-Layer Thickness on Cylinder Generated Shock-Wave/Turbulent Boundary-Layer Interactions, Part II: Experiments," 2018 AIAA Aerospace Sciences Meeting, AIAA Paper 2018-824, Kissimmee, FL, January 8-12, 2018.

[8] Combs, C. S., Kreth, P. A., Schmisseur, J. D., and Lash, E. L., "An Image-Based Analysis of Shock-Wave/Boundary-Layer Interaction Unsteadiness," AIAA Journal, 56(3), March 2018.

[9] Leidy, A.N., Neel, I.T., Bowersox, D.W., and Schmisseur, J.D., "Influence of Perturbations on 3-D Hypersonic Shock/Laminar Boundary Interactions," 55th AIAA Aerospace Sciences Meeting, AIAA Paper 2017-1685, Grapevine, TX, January 9-13, 2017.

[10] Danehy, P.M., Ivey, C.B., Inman, J.A., Bathel, B.F., Jones, S.B., McCrea, A.C., Jiang, N., Webster, M., Lempert, W., Miller, J., and Meyer, T., "High-Speed PLIF Imaging of Hypersonic Transition over Discrete Cylindrical Roughness," 48th AIAA Aerospace Sciences Meeting, AIAA Paper 2010-703, Orlando, FL, January 4-7, 2010.

[11] Berry, S.A., Auslender, A.H., Dilley, A.D., and Calleja, J.F., "Hypersonic Boundary-Layer Trip Development for Hyper-X," Journal of Spacecraft and Rockets, 38(6), pp. 853-864, November-December 2001.

[12] Combs, C.S., Schmisseur, J.D., Bathel, B.F., and Jones, S.B., "Unsteady Analysis of Shock-Wave/Boundary-Layer Interaction Experiments at Mach 4.2 Edge Conditions," submitted to AIAA Journal, November 2018.

[13] Combs, C.S., Schmisseur, J.D., Bathel, B.F., and Jones, S.B., "Analysis of Shock-Wave/Boundary-Layer Interaction Experiments at Mach 1.8 and Mach 4.2 Edge Conditions," 57th AIAA Aerospace Sciences Meeting, San Diego, CA, January 6-11, 2019.

[14] Micol, J. R., "Langley Aerothermodynamic Facilities Complex: Enhancements and Testing Capabilities," 36th AIAA Aerospace Sciences Meeting, AIAA Paper 1998-147, Reno, NV, January 1998.

[15] Berger, K., Rufer, S., Hollingsworth, K., and Wright, S., "NASA Langley Aerothermodynamics Laboratory: Hypersonic Testing Capabilities," 53rd AIAA Aerospace Sciences Meeting, AIAA Paper 2015-1337, Kissimmee, FL, January 5-9, 2015.

[16] Bathel, B.F., Danehy, P.M., Inman, J.A., Watkins, A.N., Jones, S.B., Lipford, W.E., Goodman, K.Z., Ivey, C.B., and Goyne, C.P., " Hypersonic Laminar Boundary Layer Velocimetry with Discrete Roughness on a Flat Plate," 40th AIAA Fluid Dynamics Conference, AIAA Paper 2010-4998, Chicago, IL, June 28 – July 1, 2010.
[17] Willert, C., Stasicki, B., Klinner J., and Moessner, S., "Pulsed operation of high-power light emitting diodes for imaging flow velocimetry," Measurement Science and Technology, v. 21, 2010.
[18] Willert, C. E., Mitchell, D. M., "An assessment of high-power light-emitting diodes for high frame rate schlieren imaging," Experiments in Fluids, v. 53(2), August 2012.
[19] Rasband, W.S., *ImageJ*, U. S. National Institutes of Health, Bethesda, Maryland, USA, https://imagej.nih.gov/ij/, 1997-2018.
[20] Li, K. "The image stabilizer plugin for ImageJ," http://www.cs.cmu.edu/~kangli/code/Image_Stabilizer.html, February, 2008.
[21] Dolling, D.S., and Bogdonoff, S.M., "Blunt Fin-Induced Shock Wave/Turbulent Boundary-Layer Interaction," AIAA Journal, v. 20(12), December 1982.
[22] Anderson Jr., J.D., *Hypersonic and High-Temperature Gas Dynamics, 2nd ed.*, American Institute of Aeronautics and Astronautics, AIAA Education Series, Reston, VA, 2006.